applied sciences

MDPI

Article

An Experimental Strain-Based Study on the Working State of Husk Mortar Wallboards with Openings

Xuesong Cai [1], Shijun Sun [2,*] and Guangchun Zhou [3]

[1] Department of Geotechnical Engineering, Tongji University, Shanghai 200092, China; caixiaoshuai@tongji.edu.cn
[2] Key Laboratory of Ministry of Industry and Information Technology for Human Settlement Environmental Science and Technology School of Architecture, Harbin Institute of Technology, Harbin 150090, China
[3] Key Lab of Smart Prevention and Mitigation of Civil Engineering Disasters of the Ministry of Industry and Information Technology, Harbin Institute of Technology, Harbin 150090, China; gzhou@hit.edu.cn
* Correspondence: sunsj@hit.edu.cn

Received: 29 November 2019; Accepted: 17 January 2020; Published: 19 January 2020

Abstract: Rice husks as common agricultural remnants with low density and good thermal conductivity properties have been used in infill walls in the northern area of China. Accordingly, many tests and numerical simulations were conducted to address a difficult issue, the inaccurate estimation on the lateral load-bearing capacity of different types of husk mortar energy-saving (HMES) wallboards. The difficulty has not been overcome so far, implying that the novel methods are anticipated to achieve the accurate estimation. This paper tests the full-scale HMES wallboards with different openings and obtains the strains at the points distributed on the wallboard sides. The experimental strains are modeled as the approximate strain energy values to produce the characteristic parameter of the HMES wallboard's stressing state. Furthermore, the inherent working state characteristic points of HMES wallboards are revealed from the evolution of the characteristic parameter called as the normalized approximate strain energy sum, leading to the redefinition of the failure loads for the HMES wallboards. Finally, it investigates the stressing state mode evolution of the HMES wallboard around the failure loads. The achieved results provide the reference to the accurate estimation of the bearing capacity of the HMES wallboards.

Keywords: husk mortar wallboard; experiment; lateral strength; strain; failure load

1. Introduction

To address the global issues of the warming climate and pollution, many countries have set "energy conservation" and "environmental protection" goals in recent decades. Meanwhile, many countermeasures have been taken based on the individual national conditions [1]. For instance, China banned or limited construction materials that contaminate the environment, such as clay bricks and natural woods [2], and encouraged energy-saving and environmentally friendly construction materials through policies and subsidies [3]. As a result, many new types of structural components have been developed, inclusive of rice husk and wheat husk wall panels. Commonly, energy-saving construction components are composite so that their working behavior or working mechanism are complicated and their load-bearing capacity is difficult to be accurately estimated, particularly, for their seismic performance [4,5]. The following makes an overview of the relative research results.

In the respect of experimental investigations, monotonic loading tests, quasi-static tests, and shaking table tests on different types of infill walls have been performed in recent years [6–8]. Although the tests could verify the analytical results of the proposed methods, they also presented the great variation of infill walls in configuration, material property, and manufacture of composite components.

Likewise, Peng et al. [9] conducted three cyclic experiments of infill walls with a UHPC (Ultra high performance concrete) layer and a reinforced polymer mortar layer. The UHPC layer improved a typical historical squat wall's resistance by 193%, cracking load by 127%, and ultimate deformation by 109%. Dong et al. [10] used reinforced mortar cross strips to strengthen the masonry walls and the quasi-static test results showed that such strengthening method was an effective way to improve the shear capacity and seismic performance of masonry walls. Similarly, pre-stressing technology was used by Chi et al. [11] in fully grouted concrete masonry wall systems to promote its seismic performance. Through the parameters including displacement ductility, stiffness degradation, energy dissipation, and equivalent viscous damping, the test results verified the advantages of the pre-stressing technology. Moreover, from the shaking table test of a 5-story prototype structure with a reinforced concrete frame and unreinforced masonry, Hashemi et al. [12] found that the unreinforced masonry infill wall provided a significant contribution to the strength and ductility of the structure and should be considered in both analysis and design.

In the respect of numerical modelling, finite element (FE) analysis was widely used to study the mechanical properties of infill walls [13–16]. Betti et al. [17] built both plasticity model and smeared cracking/crushing model to analyze the working behavior of historic buildings with infill walls under seismic loading. Bartoli et al. [18] suggested the multi-level approach to assess the static and seismic capacity of historic masonry towers, and performed three levels of evaluation, namely LV1 (analysis at territorial level), LV2 (local analysis), and LV3 (global analysis). Ferrero et al. [19] calibrated the numerical model according to the eigenvalue analysis and the test of the dynamic identification. Then the nonlinear static analyses were performed to evaluate the seismic response of the structure, which obtained the reliable parameters for modeling infill walls. In the recent years, Zhou et al. [20] built the neural network mode of laterally loaded masonry walls to estimate their failure loads and failure patterns. Zhang et al. [21] used the cellular automata approaches to predict the cracking patterns of masonry wallets under vertical loads. Huang et al. [22] developed a generalized strain energy density (GSED)–based method and revealed the relationship between the failure loads of the base/test masonry wall panels.

The available data regarding full-scale wallboard's load capacity remains limited. Investigations on the strain data for analyzing structural behavior are particularly scarce. Most of these researches focus on the load and displacement data. No experimental program has yet, to the authors' knowledge, been undertaken with strain analysis method on husk mortar energy-saving (HMES) wallboards. The tests and numerical analyses mentioned above obviously reflect two issues: (1) A reasonable numerical model would not have been established due to the configuration complexity of HMES wallboards. As a result, an accurate prediction for the ultimate strength of HMES wallboards has not been achieved by the existing analytical theories and methods. (2) The displacement data and force data were fully utilized, but the strain data were not fully applied. The structural working features embodied in the strain data have not been explored. Both problems implied that new theories and methods should be developed to solve them [23]. Zhou's structural stressing state theory explored a new way to deeply understand the structural working behavior features from the experimental strain data and provided a proper method to definite structural failure load [24,25]. In view of Zhou's theory, this paper investigated the structural working state of full-scale HMES wallboards with different openings. It was considered that the structural working state related to the individual working states of the local zones within the wallboard. So the strain values with the load increase were measured at the points uniformly distributed on both sides of the wallboard. The study revealed the inherent leap characteristics implied in the working states of wallboards and redefined their failure loads. An empirical relationship among the experimental failure loads of the wallboards was derived based on the failure characteristics of the wallboards. which could provide the reference to the accurate prediction of the wallboards' load-bearing capacity. In addition, a new way was explored to apply the enormous amount of experimental strain data to structural analysis.

2. HMES Wallboards and Testing Preparation

2.1. The Configuration and Size of the HMES Wallboards

The structure of HMES wallboards is briefly described since it has already been reported in detail [26]. The husk mortar is made of cement, sand, husks, water, and additive. This panel can be used to the multi-story and high-rise reinforced concrete frame construction as facade, its overall size is the same with the external wall. The wall panel consists of two husk mortar surface layers, and two insulation layers (benzene or asbestos), and an air layer inside. The two surface layers are connected by the vertical and horizontal reinforced ribs.

Figure 1 shows the sectional structure. An HMES wallboard consists of three parts: two surface layers, two benzene board layers, and one cavity layer. The vertical and transverse ribs are arranged in the interior of the wallboard, and the reinforcing bars are arranged between the two surfaces. The metal mesh is in the surface layer. The benzene board is cut into small pieces, and between two pieces, there is a gap for a rib. The insulation mortar is poured between the surface layer and the benzene board layer for bonding and fixation. The vertical reinforced bar, the metal mesh in the surface layer, and the transverse pull bar are bonded at their intersection, constituting a three-dimensional metal grid. The metal rings are set in the upper edge of the wallboard for convenient hoisting and transport. Figure 2 shows the wallboard products.

Figure 1. The wallboard products.

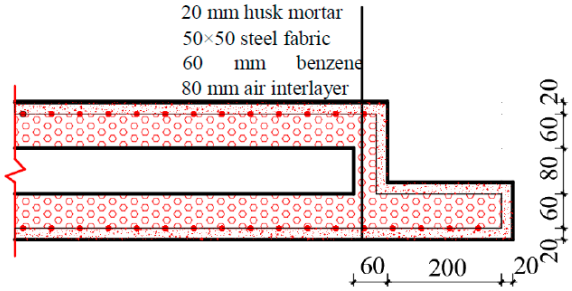

Figure 2. Section of husk mortar energy-saving (HMES) wallboard.

As shown in Figure 3, an experimental building with the HMES wallboards was built in 2008, and some houses were built later with such wallboards according to needs of local construction. The dimensions of HMES wallboards are determined by column space, height of the floor, and dimensions of windows and doors.

In this experiment, two groups of full-scale HMES wallboards are manufactured based on the norms of practical engineering. The sizes, lateral loading cases, and numbers of the wallboards are shown in Table 1. Considering their low lateral bearing capacity, which is unsuitable for cyclic loading testing, wallboards 1-3, 1-4, 2-1, 2-2, 2-3, and 2-4 with openings are subjected to monotonic loads only. For purposes of comparison with the monotonic loading cases, wallboards 1-1 and 1-2 are subjected to cyclic loads.

Figure 3. Construction process.

Table 1. The configurations and sizes of the experimental HMES wallboards.

Configuration & Size Dimensions in mm	Group 1		Group 2	
	No.	Lateral Loading Case	No.	Lateral Loading Case
Intact Wallboard 3300 × 2800 × 250	1-1	cyclic	2-1	monotonic
Window opening: 1500 × 1600 3300 × 2800 × 250	1-2	cyclic	2-2	monotonic
Door opening: 900 × 2100 2400 × 2800 × 250	1-3	monotonic	2-3	monotonic
Window opening:1500 × 1600 Door opening: 900 × 2100 3300 × 2800 × 250	1-4	monotonic	2-4	monotonic

2.2. Experimental Device and Loading Scheme

This experiment was carried out at the Heilongjiang Institute of Science and Technology, China. The experimental device is shown in Figure 4. The vertical load was applied by mechanical jacks, and the horizontal load was applied by a hydraulic servo actuator, which was installed in the same plane as the specimen. To facilitate lifting, a steel groove was designed and fixed at the bottom of the tested wallboard by pouring concrete. Two jacks were installed for connecting the specimen and the base. In this way, the base of the specimen was fixed during the test. A pair of two tie rods were installed on the loading end of the horizontal actuator; a cyclic load could be realized with such a loading device. The horizontal cyclic load and monotonic loads were supplied by a 500 kN actuator. As shown in Figure 5, the loading was force controlled for the cyclic loading case as well as the monotonic loading case. The loading scheme was composed of applying incremental multiples of 5.0 kN until the test was terminated for the specimen 1-1, specimen 1-2, specimen 2-1, and specimen 2-2. As for specimen 1-3, specimen 1-4, specimen 2-3, and specimen 2-4, the incremental force was 3.0 kN. In addition, the specimen was exposed to an axial load of 30 kN at the top surface that was applied by two hydraulic jacks on the rigid distribution beam, which represented the gravity load and remained constant throughout the test. The force controlled scheme was chosen over displacement controlled scheme for the reason that force and strain energy data were significant in the analysis of strain energy, which is applied in Section 4.3. As the load capacities of the HMES wallboards with different sizes are usually different, the load increments of specimen 1-1 and 1-2 are set 5.0 kN while the load increments of specimen 1-3 and 1-4 are set 3.0 kN.

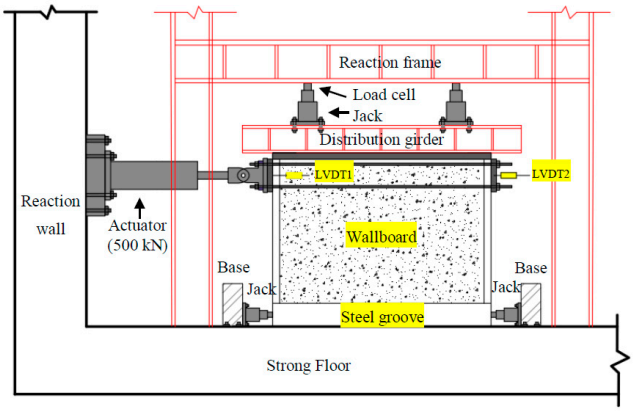

Figure 4. Overview of the test setup and instrumentation.

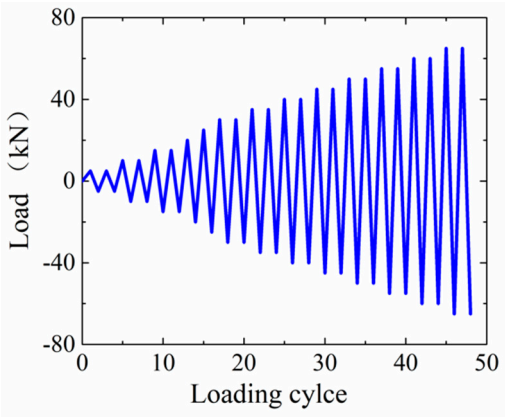

Figure 5. The loading scheme for the cycle test.

2.3. Measuring Scheme

During the HMES wallboard experiment, the measuring data include the horizontal load values and the corresponding displacements at the loading position. To measure strain, standard strain gauges specific to concrete are adopted. The strain signal is recorded by the electrical resistance strain indicator per second. The strain data are collected at the peak point of every loading process. Notably, this experiment specifically considers the measurement of the strain values: (1) the strain values indicate the local behavior of the wallboard; thus, they are recorded in three directions at the representative positions on both sides of the wallboard; and (2) the working state mode of the wallboard can be numerically described by the strain values at uniformly distributed locations. Hence, for instance, the strain layout of wallboard 1-1 is designed as shown in Figure 6.

Two linear variable differential transducers (LVDTs) were placed at the top sections of the specimens to measure longitudinal deformations along the loading direction. All measurements of the load cells, displacement transducers, and strain gauges were recorded by a computer data logger.

The principal strains, the shear strains, and the inclinations of the principal strains were calculated based on the strain data, and the maximum values of the strains under each level of loading were applied for calculating the strain energy.

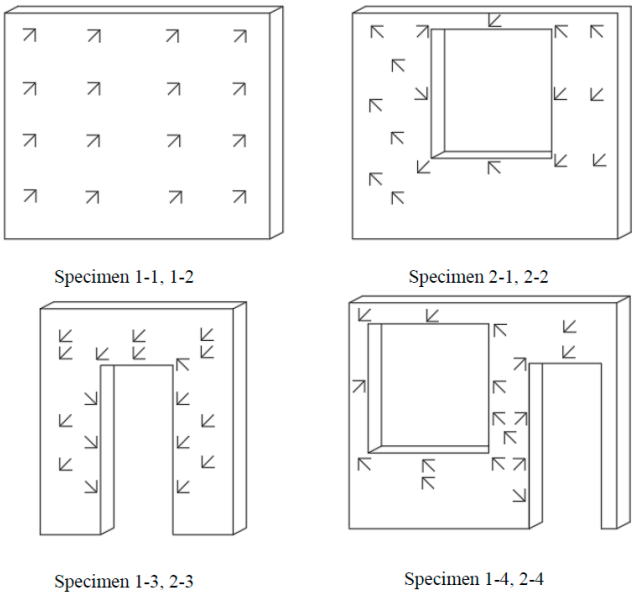

Figure 6. The layout of the strain gauges.

3. The Experimental Results

3.1. Test Results of Material Test

As shown in Figure 7, material tests of husk mortar were carried out according to the requirements of the Standard of Testing of Mechanical Properties of Ordinary Concrete [27]. The compressive strength of husk mortar is 18.6 MPa, measured on a set of 3 cubic samples. Several key parameters of husk mortar, such as compressive strength, density, water content, thermal conductivity, and elastic modulus are listed in Table 2.

Figure 7. Cube for material test.

Table 2. Mechanical properties of husk mortar.

Cube Number	Compressive Strength	Density	Water Content	Thermal Conductivity	Elastic Modulus
	MPa	kg/m^3	%	W/(m × k)	MPa
A	21.20	1733	3.1	0.394	
B	14.13	1467	3.5	0.233	4976
C	20.60	1633	3.4	0.380	

3.2. Test Results of HMES Wallboords

Typically, experimental data are analyzed to have a reliable and accurate formula for calculating the ultimate/failure load and the structural parameters corresponding to some working behavior

characteristics. For the experimental data related to this study, such an analysis was also performed [20]. However, it seems that the experimental records of cracking phenomena and strain values have not been fully studied thus far. A great amount of unseen knowledge is certainly implied in the experimental data, and only some innovative method is necessary to reveal this knowledge. Here, the analysis of the experimental data focuses on the cracking mechanism and the stressing state of the wallboard from a structural perspective based on the concept of the structural stress state.

Figure 8 draws the failure patterns of the eight wallboards based on the experimental observations. It should be noted that the concrete bonding failure occurs in the steel groove of specimen 2-1. Through upgrading the strength of the concrete, which was poured in the steel groove, similar failure patterns do not reappear in the following tests.

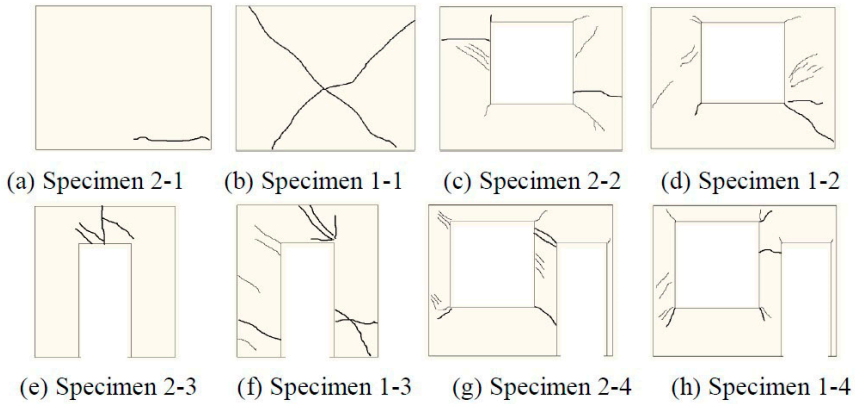

Figure 8. The experimental cracking patterns of the HMES wallboards.

The experimental records of the HMES wallboards corresponding to Table 1 are summarized in Table 3.

Table 3. The experimental records of the HMES wallboards.

Wallboard No.	Lateral Loading Condition	CL-O (kN)	FL-O (kN)	UL (kN)
1-1	cyclic	54.29	88.48	93.20
1-2	cyclic	39.73	69.14	78.54
1-3	monotonic	36.00	42.00	62.31
1-4	monotonic	18.61	27.67	47.52
2-1	monotonic	-	-	-
2-2	monotonic	41.50	78.81	81.26
2-3	monotonic	20.60	42.00	47.55
2-4	monotonic	21.70	39.00	42.00

Note: CL-O is the load corresponding to the first cracking, as based on observation; FL-O is the load corresponding to the formation of a complete cracking pattern, as based on observation; and UL is the ultimate load at the end of the test.

From the experimental phenomena of the HMES wallboards, the following comment regarding their future design and engineering application can be made: the first crack occurs at the weakest zone in the wallboards where the maximum stress exists. Clearly, the weakest zone is dependent on the configuration of the wallboard. Importantly, the cracking pattern of the wallboard provides a reference for its configurational improvement. For instance, for the wallboard with a door opening, the cracking zone between the top edges of the wallboard and the door indicates that some strengthening measures may be taken there; additionally, some strengthening measures may be taken in the cracking zone between the door and window openings. Therefore, efforts should be made to ensure a shearing working state for the engineering application of this wallboard.

4. Data Analysis

4.1. FE Model

As shown in Figure 9, the HMES wallboards were modeled in ABAQUS/Explicit with C3D8R elements. The C3D8R element is a general-purpose linear brick element, with reduced integration (1 integration point) [28]. The shape functions are the same as for the C3D8 element. In the force-control loading pattern, a uniform increasing pressure is imposed on the top face of specimens gradually until failure occurs. The load capacity of two insulation layers is neglected in the FE (Finite element) model.

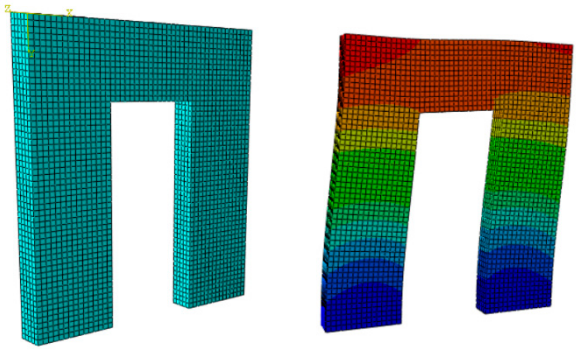

Figure 9. FE model and deformation pattern of specimen 1-3.

The elastic modulus of husk mortar was set as 4976 MPa according to the test results mentioned above. A preliminary FE model with elastic modulus of husk mortar was established to validate the results of HMES wallboards.

Figure 10 shows that there is a relatively reasonable agreement between numerical and test values at the initial stage of the load displacement curve. Such results verify the accuracy of test methods and test results in the elastic range. However, the numerical and test results do not match well after the displacement reaches 6.41 mm. When the specimen 1-3 enters the plastic stage, the elastic constitutive model of husk mortar cannot reflect the plastic behavior of HMES wallboards. A reasonable constitutive model should be adopted for plastic analysis. This issue requires additional research.

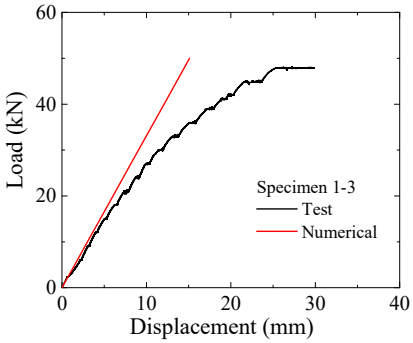

Figure 10. Numerical and test results of specimen 1-3.

4.2. The Characteristic Parameters

Typically, the first cracks are a local failure of the wallboard. With cracking propagation, local failure becomes structural failure. This development might raise the question of how to define structural failure based on the propagation of local failure/cracking, that is, how to delineate the boundary between structural and local failures. In other words, the stressing state of a structure should be expressed by the response data of key points from the experimental measurement or numerical simulation. This issue leads to an updated definition of structural failure. In this definition, the structural failure state is

defined as the working state after the structure loses its stable/normal working state, which is not a structural collapse corresponding to the ultimate load. Here, the wallboards are analyzed to reveal their unseen working characteristics and to define their failure loads based on an empirical modelling of the experimental data.

First, a characteristic parameter $E_{j,\text{norm}}$ is defined as the normalized approximate strain energy (NASE) sum of the wallboard to the jth load level F_j; that is,

$$E_{j,\text{norm}} = \frac{\sum_{i=1}^{N} E_{ij}}{E_M}, \qquad E_{ij} = \frac{1}{2}\overline{E}\varepsilon_{ij}^2 \tag{1}$$

where E_{ij} is the ASE value of the ith measuring point to the jth load increment; N is the number of measuring points distributed on the wallboard; E_M is the maximum sum of strain energy among the measuring points to the individual load increments or the ASE sum to the last (Mth) load increment; $\overline{E}$ is the elastic modulus; and ε_{ij} is the strain value at the ith point to the jth load increment.

For Equation (1), two points must be indicated:

(a) E_{ij} is just an approximate strain energy parameter of the wallboard since it is calculated using a limited number of experimental strain values. Furthermore, $E_{j,\text{norm}}$ approximately reflects the global behavior of the wallboard under lateral load. However, $E_{j,\text{norm}}$ might better reflect the real working behavior of the wallboard than conventional numerical simulation because of the direct application of experimental data.

(b) At present, a large amount of experimental strain data has not been fully used in the field of structural analysis. Hence, the introduction of $E_{j,\text{norm}}$ represents a methodological attempt to reflect some unseen global working behavior of the wallboard (it could be as a structure) by applying experimental strain values.

4.3. Characteristic Curve

For the seven specimens for which the uniformly distributed strain values are measured, Figure 11a–g draws their characteristic curves of the relationship between F_j and $E_{j,\text{norm}}$. To be specific, CP stands for the crack point, and FP stands for the failure point, which is defined as the point where the slope of the curve changes greatly.

Figure 11 shows that the seven specimens basically embody a similar feature of three working stages, particularly the failure loads dotted in the $F_j - E_{j,\text{norm}}$ curves. Three working stages can be seen in Figure 11, together with the experimental observations:

In Figure 11a, before the load reaches 55.0 kN, specimen 1-1 works in an elastic state. Afterwards, specimen 1-1 enters an elastic-plastic working state, as the inflection point from a linear shape to a nonlinear shape in the $F_j - E_{j,\text{norm}}$ curve emerges. As the load changes from 55.0 kN to 65.0 kN, specimen 1-1 works in an elastic-plastic state due to the propagation of the first crack and the appearance of other cracks. Notably, however, specimen 1-1 maintains a stable mode of strain energy distribution in these two working states. When the load reaches 65.0 kN, the second inflection point in the $F_j - E_{j,\text{norm}}$ curve emerges, at which point specimen 1-1 cannot maintain a stable mode of strain energy distribution before collapsing. According to the definition in reference [29,30], defining the first inflection point as the cracking load, and the second inflection point as the failure load, it can be seen from Figure 11a that 55.0 kN is the crack load of specimen 1-1, 65.0 kN is the failure load of specimen 1-1, and 93.2 kN is the ultimate load of specimen 1-1.

Similarly, in Figure 11b the crack load, failure load, and ultimate load of specimen 1-2 are 20.5 kN, 69.8 kN, and 78.6 kN, respectively. In Figure 11c the crack load, failure load, and ultimate load of specimen 1-3 are 17.9 kN, 42.0 kN, and 62.3 kN, respectively. In Figure 11d the crack load, failure load, and ultimate load of specimen 1-4 are 18.1 kN, 45.4 kN, and 47.5 kN, respectively. In Figure 11e the crack load, failure load, and ultimate load of specimen 2-2 are 21.5 kN, 74.6 kN, and 81.3 kN,

respectively. In Figure 11f the crack load, failure load, and ultimate load of specimen 2-3 are 21.3 kN, 42.5 kN, and 47.6 kN, respectively. In Figure 11g the crack load, failure load, and ultimate load of specimen 2-4 are 27.5 kN, 36.6 kN, and 42.0 kN, respectively.

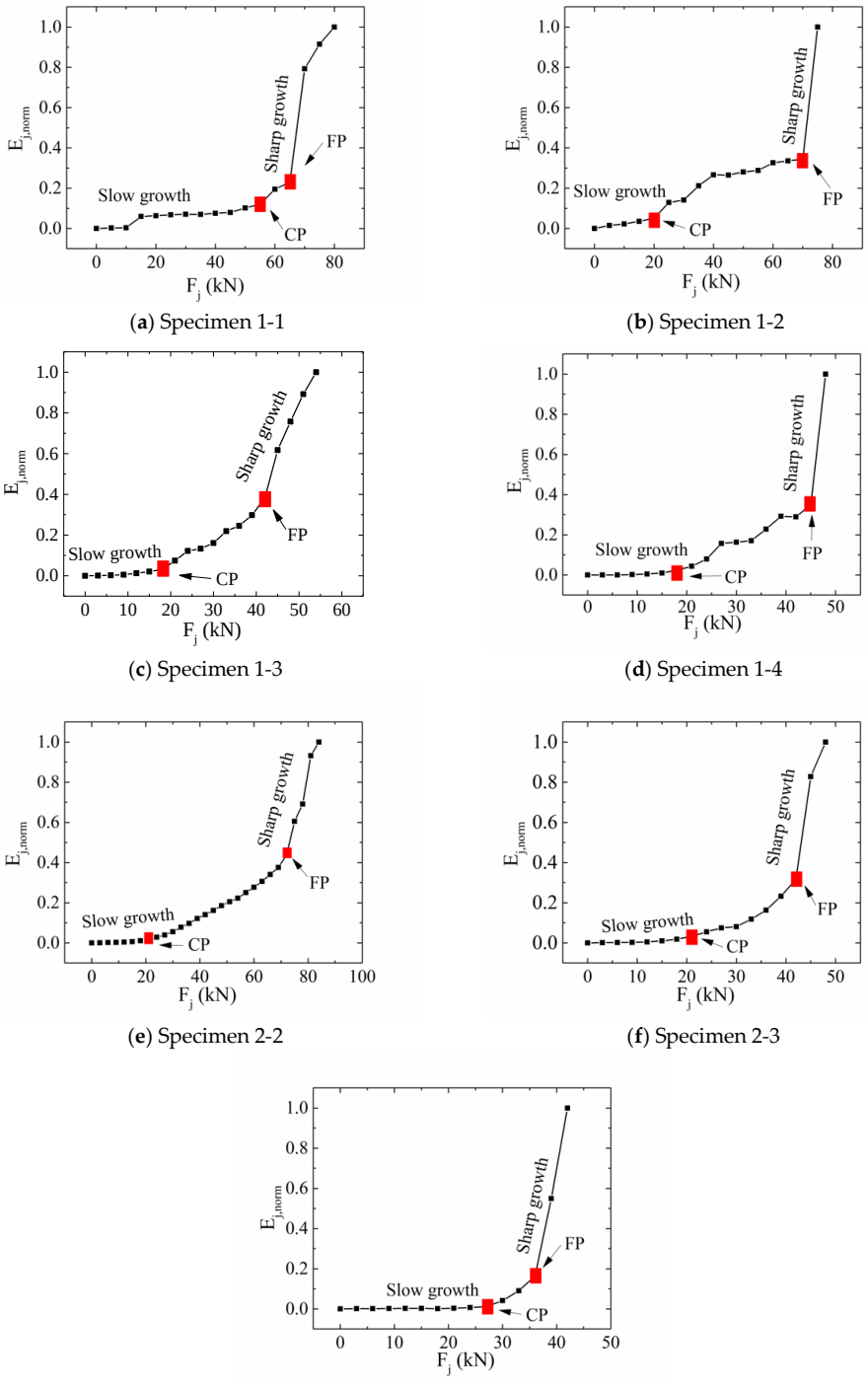

(**a**) Specimen 1-1 (**b**) Specimen 1-2

(**c**) Specimen 1-3 (**d**) Specimen 1-4

(**e**) Specimen 2-2 (**f**) Specimen 2-3

(**g**) Specimen 2-4

Figure 11. The $F_j - E_{j,\mathrm{norm}}$ curves of the specimens. Note: CP is the cracking load point; FP is the failure load point.

Here, three points must be emphasized: (1) FP exists in the $F_j - E_{j,\mathrm{norm}}$ curve of every specimen, as shown in Figure 11. (2) FP emerges in the elastic-plastic working stage of the specimen. (3) The working states of the wallboard are different before and after the appearance of FP. The former

state is relatively stable and maintains a relatively constant mode/pattern, while the latter state is unstable/changeable with the load increment. Therefore, based on the characteristic point in the $F_j - E_{j,\text{norm}}$ curve, the response of a wallboard to a load increment can be divided into two working states: the stable/normal working state occurring until the characteristic point and the unstable/failure working state from the characteristic point to the collapse of the wallboard. The failure load is defined as the load value at the characteristic point.

The results of the crack load and failure load derived from the strain data are consistent with the results based on observations, as shown in Figure 12. Actually, the crack results based on observation requires manpower and depends on the experimental environment. Therefore, the crack load cannot be defined clearly in this way. Moreover, when the crack occurs in the initial stage, the width of the crack is not large enough for observation. With strain analysis method, the initial stage of crack could be captured reasonably.

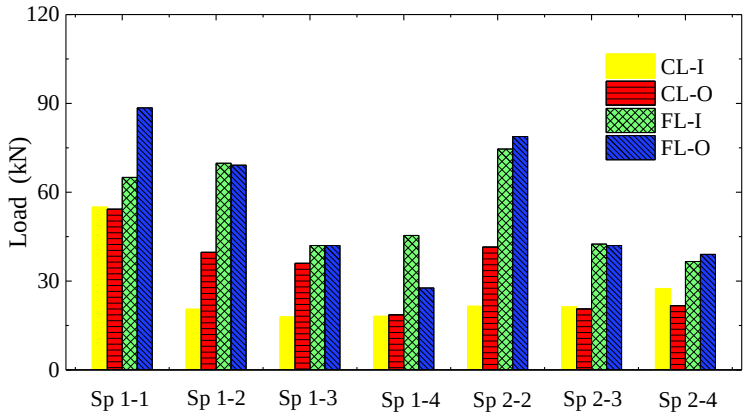

Figure 12. Crack load and failure load with different methods. Note: CL-O is the load corresponding to the first cracking, as based on observation; FL- O is the load corresponding to the formation of a complete cracking pattern, as based on observation; CL-I is the cracking load based on the strain analysis; and FL-I is the failure load based on the strain analysis.

The analysis of the strain data provides a proper way to judge whether cracks occur/propagate in the specimen. The appearance of CP marks that cracks have occurred and have begun to propagate in the specimen.

4.4. MK Criterion

To distinguish the stressing state jump of the structure via the $F_j - E_{j,\text{norm}}$ curve, the MK (Mann-Kenddall) method is applied [24]. The function of F_j is monotonically increasing because the loading scheme is force controlled. The characteristic point defined by the MK method can be used to describe the structural stressing state.

The sequence of E_i is statistically independent. Then, a statistical quantity d_k at the kth load can be defined as

$$d_k = \sum_{i}^{k} m_i \ (2 \le k \le n) \quad m_i = \begin{cases} +1 & E(i) > E(j) \ (1 \le j \le i) \\ 0 & \text{otherwise} \end{cases} \tag{2}$$

where m_i is the cumulative number of the samples and $+1$ indicates adding one to the existing value if the inequality on the right side is satisfied for the jth comparison. Next, calculate the mean value $E(d_k)$ and $Var(d_k)$ of d_k:

$$\begin{gathered} E(d_k) = k(k-1)/4 \quad (2 \le k \le n) \\ Var(d_k) = k(k-1)(2k+5)/72 \quad (2 \le k \le n) \end{gathered} \tag{3}$$

A new statistical quantity UF_k is defined by Equation (4), and the $UF_k - F$ curve can be plotted.

$$UF_k = \begin{cases} 0 & k = 1 \\ d_k - E(d_k) \ \sqrt{Var(d_k)} & 2 \le k \le n \end{cases} \quad (4)$$

For the inverse sequence of E_i, the same steps are conducted to yield the $UB_k - F$ curve. The intersection point of the $UF_k - F$ and $UB_k - F$ curves is the characteristic point of the structural stressing state. In this way, the failure point can be defined properly.

For example, the characteristic point of specimen 1-3 was analyzed, as shown in Figure 13.

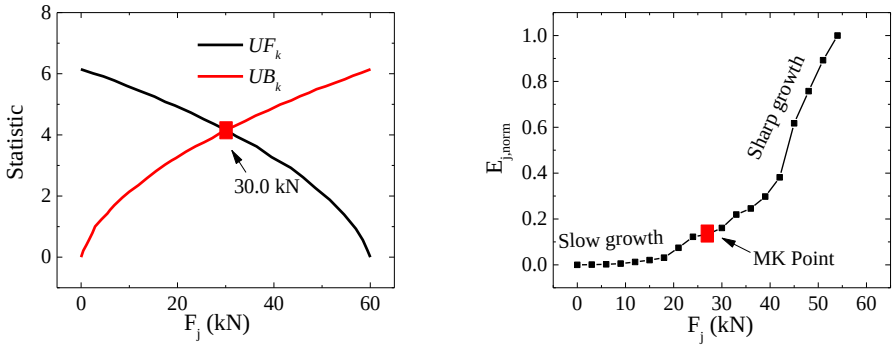

Figure 13. Crack load defined by the MK method.

The other six specimens were correspondingly analyzed with the MK method, and the loads at the MK point are recorded in Figure 14. When CL-O is considered as the standard value, then the load value derived from the MK method is closer than CL-I, as seen from Figure 14.

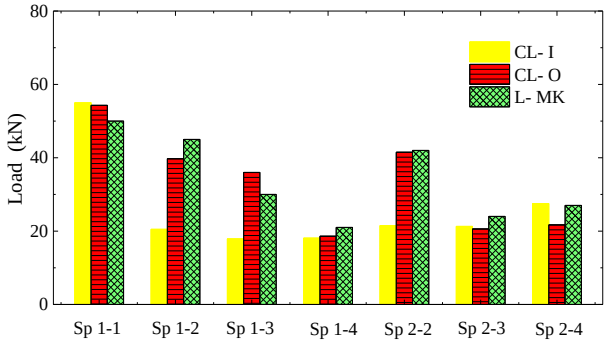

Figure 14. Loads defined by the MK method.

4.5. Structural Stress State

The sum of the strain energies can reflect the overall working state of the specimens. Moreover, the change in the stress state, which reflects the strain distribution, can be derived from the strain data as well. To be specific, Figure 15 shows that strain distribution of specimen 1-3.

Figure 15 indicates that the jump features of the stressing state modes are consistent with those revealed in Figure 11. Figure 15 shows sudden and sharp increases at 18.0 kN and 45.0 kN, with the latter more apparent. Thus, it can be inferred that when the load reaches 21.0 kN and 48.0 kN, the stressing state of the specimen changes to another stressing state sub-mode. Of further note is that the stressing state remains stable between the first characteristic point (P1) and the second characteristic point (P2), whereas the stressing state cannot maintain stability after the second characteristic point.

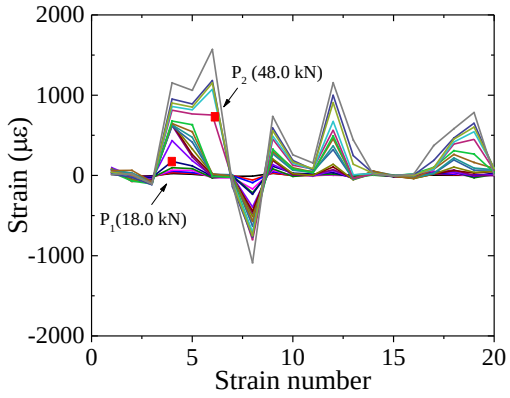

Figure 15. The changing features of strain-based stressing state modes for specimen 1-3.

5. Summary and Conclusions

This study attempts an innovative application of experimental strain data to investigate the working states of HMES wallboards with openings based on the concept of the structural stress state. It should be noted that such investigation is suitable for in-plane shear behavior of infill walls subjected to the monotonic and cyclic loading. Issues with more complex loads, different stiffnesses of joints, rigidity of joining elements, and various configurations require additional research. The investigation draws the following conclusions:

The experimental strains can be transferred into the approximate strain energy values to build the parameter (the NASE sum) characterizing the HMES wallboard's working state. The evolution of the NASE sum will present the characteristic points of the HMES wallboard's working state, i.e., the crack load and failure load. Then, the MK method is applied to detect the characteristic load from $E_{j,\mathrm{norm}} - F_j$ curve and finds out the crack load (L-MK). The comparison of the characteristic loads verify the rationality of the crack loads (L-MK). The modeling method of experimental strains and the MK method could derive the rational and accurate crack loads and provide the rational reference to update the design code of HMES wallboards. Moreover, it provides the method to analyze the local and whole working behaviors of HMES wallboards.

Author Contributions: Conceptualization, S.S.; Data curation, X.C.; Investigation, X.C.; Methodology, X.C.; Software, X.C.; Supervision, S.S.; Validation, G.Z.; Writing—review & editing, S.S. All authors have read and agreed to the published version of the manuscript.

Funding: This research received no external funding.

Conflicts of Interest: The authors declare no conflict of interest.

References

1. Leslie, P.; Pearce, J.M.; Harrap, R.; Daniel, S. The application of smartphone technology to economic and environmental analysis of building energy conservation strategies. *Int. J. Sustain. Energy* **2012**, *31*, 295–311. [CrossRef]
2. Chen, R. *Research and Application of Rice-Hull Mortar Lightweight Composite Wall Panel*; Harbin Institute of Technology: Harbin, China, 2010.
3. Cai, X.S. *In-Plane Mechanical Properties of New Energy-Saving Infill Walls*; Harbin Institute of Technology: Harbin, China, 2014.
4. Marques, R.; Lourenço P, B. Structural behaviour and design rules of confined masonry walls: Review and proposals. *Constr. Build. Mater.* **2019**, *217*, 137–155. [CrossRef]
5. Lourenco, P.B.; Milani, G.; Tralli, A.; Zucchini, A. Analysis of masonry structures: Review of and recent trends in homogenization techniques. *Can. J. Civ. Eng.* **2007**, *34*, 1443–1457. [CrossRef]
6. Ju, R.S.; Lee, H.J.; Chen, C.C.; Tao, C.C. Experimental Study on Separating Reinforced Concrete Infill Walls from Steel Moment Frames. *Constr. Steel Res.* **2012**, *71*, 119–128. [CrossRef]

7. Gu, X.; Wang, L.; Zhang, W.; Cui, W. Cyclic behaviour of hinged steel frames enhanced by masonry columns and/or infill walls with/without CFRP. *Struct. Infrastruct. Eng.* **2018**, *14*, 1–16. [CrossRef]
8. Jurko, Z.; Vladimir, S.; Ivica, G. Cyclic Testing of a Single Bay Reinforced Concrete Frames with Various Types of Masonry Infill. *Earthq. Eng.* **2013**, *41*, 1131–1149.
9. Peng, B.; Wei, S.; Long, L.; Zheng, Q.; Ma, Y.; Chen, L. Experimental Investigation on the Performance of Historical Squat Masonry Walls Strengthened by UHPC and Reinforced Polymer Mortar Layers. *Appl. Sci.* **2019**, *9*, 2096. [CrossRef]
10. Dong, K.; Sui, Z.-A.; Jiang, J.; Zhou, X. Experimental Study on Seismic Behavior of Masonry Walls Strengthened by Reinforced Mortar Cross Strips. *Sustainability* **2019**, *11*, 4866. [CrossRef]
11. Chi, B.; Yang, X.; Wang, F.; Zhang, Z.; Quan, Y. Experimental Investigation into the Seismic Performance of Fully Grouted Concrete Masonry Walls Using New Prestressing Technology. *Appl. Sci.* **2019**, *9*, 4354. [CrossRef]
12. Hashemi, A.; Mosalam, K.M. Shake-table Experiment on Reinforced Concrete Structure Containing Masonry Infill Wall. *Earthquake Eng. Struct. Dyn.* **2006**, *35*, 1827–1852. [CrossRef]
13. Torelli, G.; D'Ayala, D.; Betti, M.; Bartoli, G. Analytical and numerical seismic assessment of heritage masonry towers. *Bull. Earthq. Eng.* **2019**. [CrossRef]
14. Orlando, M.; Betti, M.; Spinelli, P. Assessment of structural behaviour and seismic retrofitting for an Italian monumental masonry building. *J. Build. Eng.* **2019**, *29*, 101115.
15. Betti, M.; Vignoli, A. Modelling and analysis of a Romanesque church under earthquake loading: Assessment of seismic resistance. *Steel Constr.* **2008**, *30*, 352–367. [CrossRef]
16. Betti, M.; Orlando, M.; Vignoli, A. Static behaviour of an Italian Medieval Castle: Damage assessment by numerical modelling. *Comput. Struct.* **2011**, *89*, 1956–1970. [CrossRef]
17. Betti, M.; Galano, L.; Vignoli, A. Finite Element Modelling for Seismic Assessment of Historic Masonry Buildings. In *Earthquakes and Their Impact on Society*; Springer: Cham, Germany, 2016; pp. 377–415.
18. Bartoli, G.; Betti, M.; Vignoli, A. A numerical study on seismic risk assessment of historic masonry towers: A case study in San Gimignano. *Bull. Earthq. Eng.* **2016**, *14*, 1475–1518. [CrossRef]
19. Ferrero, C.; Lourenço, P.B.; Calderini, C. Nonlinear modeling of unreinforced masonry structures under seismic actions: Validation using a building hit by the 2016 Central Italy earthquake. *Frattura ed Integrità Strutturale* **2020**, *14*, 92–114. [CrossRef]
20. Zhou, G.; Pan, D.; Xu, X.; Rafiq, Y.M. An innovative technique for predicting failure/cracking load of masonry wall panel under lateral load. *J. Comput. Civ. Eng.* **2010**, *24*, 377–387. [CrossRef]
21. Zhang, Y.; Zhou, G.C.; Xiong, Y.; Rafiq, M.Y. Techniques for predicting cracking pattern of masonry wallet using artificial neural networks and cellular automata. *J. Comput. Civ. Eng.* **2010**, *24*, 161–172. [CrossRef]
22. Huang, Y.; Zhou, G.; Cui, L.; Zhang, K.; Zhang, M.; Huang, Q.A. Method for Predicting Failure Load of Masonry Wall Panel Based on Generalized Strain Energy Density. *J. Eng. Mech.* **2014**, *140*, 04014061. [CrossRef]
23. Shi, J.; Shen, J.; Zhou, G.; Qin, F.; Li, P. Stressing state analysis of large curvature continuous prestressed concrete box-girder bridge model. *J. Civ. Eng. Manag.* **2019**, *25*, 411–421. [CrossRef]
24. Shi, J.; Li, W.; Zheng, K.; Yang, K.; Zhou, G. Experimental Investigation into stressing state characteristics of large-curvature continuous steel box-girder bridge model. *Constr. Build. Mater.* **2018**, *178*, 574–583. [CrossRef]
25. Shi, J.; Yang, K.; Zheng, K.; Shen, J.; Zhou, G.; Huang, Y. An Investigation into working behavior characteristics of parabolic CFST arches applying structural stressing state theory. *J. Civ. Eng. Manag.* **2019**, *25*, 215–227. [CrossRef]
26. Sun, S.; Ma, D.; Zhou, G. Applications and Analysis of the Composite wall on Construction in Heilongjiang Province. *Procedia Eng.* **2015**, *118*, 160–168. [CrossRef]
27. Ministry of Construction of China. *Standard of Test Method of Mechanical Properties on Ordinary Concrete (GB/T50081-2002)*; Ministry of Construction of China: Beijing, China, 2002.
28. Abaqus, G. *Abaqus 6.11*; Dassault Systemes Simulia Corporation: Johnston, RI, USA, 2011.
29. Zhang, M.; Zhou, G.; Huang, Y.; Zhi, X.; Zhang, D.Y. An ESED Method for Investigating Seismic Behavior of Single-Layer Spherical Reticulated Shell. *Earthq. Struct.* **2017**, *13*, 455–464.
30. Zhang, M.; Parke, G.; Tian, S.; Huang, Y.; Zhou, G. Criterion for Judging Seismic Failure of Suspen-dome Based on Strain Energy Density. *Earthq. Struct.* **2018**, *15*, 123–132.